Journal of Materials Chemistry A

ROYAL SOCIETY OF CHEMISTRY

PAPER

View Article Online
View Journal | View Issue

Cite this: J. Mater. Chem. A, 2026, 14, 6934

Enhancement of the thermoelectric performance *via* defect formation and device fabrication for $Cu_{26}Ti_2(Sb,Ge)_6S_{32}$ colusite

Koichiro Suekuni, *[ab] Mei Yamamoto,[a] Susumu Fujii, [c] Pierric Lemoine, [d] Philipp Sauerschnig, [e] Michihiro Ohta, [e] Emmanuel Guilmeau [f] and Michitaka Ohtaki [ab]

A copper-based multicomponent sulphide, $Cu_{26}Ti_2(Sb,Ge)_6S_{32}$ colusite, is a promising thermoelectric material. We investigated the effects of sulphur deficiency on the crystal structure, electronic structure, and thermoelectric properties in the series $Cu_{26}Ti_2Sb_4Ge_2S_{32-x}$. By combining experiments and *ab initio* calculations, we found that sulphur deficiency induced the formation of interstitial Cu atoms in the sphalerite-like framework of $Cu_{26}Ti_2Sb_4Ge_2S_{32}$. This resulted in a decrease in the hole carrier concentration and a susbtantial enhancement of ZT up to unity at 673 K. We also fabricated a power generation device composed of the sulphur-deficient colusite, Ni–Sb-based compounds (interface material), and Ni. The maximum conversion efficiency of the device reached 3.2% with a temperature difference of 266 K.

Received 22nd October 2025
Accepted 29th December 2025

DOI: 10.1039/d5ta08599c

rsc.li/materials-a

1 Introduction

There has been growing concern about ever-increasing energy consumption and the resulting serious environmental issues. Thermal-to-electrical energy conversion techniques are important for improving energy efficiency and decreasing carbon footprint emissions. As such a technique, thermoelectric (TE) power generation, which enables the direct conversion from heat into electricity, has gained growing attention.[1] TE energy conversion is based on the Seebeck effect, in which a temperature difference causes an electromotive force (voltage). The voltage, ΔV, is proportional to the temperature difference ΔT across the solid-state device as $\Delta V = -S\Delta T$, where S is the Seebeck coefficient. To obtain a large output power, a high output voltage as well as low internal resistance are required for the device. Furthermore, low thermal conductance is a requisite characteristic for the device to decrease heat flow that does not contribute to power generation. Consequently, materials used in TE devices should have large S, low electrical resistivity, ρ, and low thermal conductivity, κ. By combining these parameters (S, ρ, and κ), the performance of TE materials can be expressed as $ZT = S^2\rho^{-1}\kappa^{-1}T$, which is referred to the dimensionless figure of merit. Here, $S^2\rho^{-1}$ is referred to the power factor, and κ is the sum of its electronic component κ_{ele} and lattice component κ_{lat}.

To achieve large-scale, cost-effective, and environmentally friendly TE applications, materials must not only be high-performing but also composed of constituent elements that are non-toxic, environmentally benign, and low-cost. Examples include Mg-based compounds ($Mg_3(Bi,Sb)_2$,[2–4] MgAgSb,[5–7] and $Mg_2(Si,Sn)$[8–10]), Half-Heusler compounds (MNiSn and MCoSb, with M = Ti, Hf, Zr, and NbFeSb),[11–13] and sulphides (Cu-based,[14–16] Bi-based,[17,18] and Ti-based compounds[19–22]). Cu-based sulphides have emerged as promising p-type TE materials, and their TE properties have been studied extensively since ~2010. The worldwide research led to significant advances in TE Cu-based sulphides (*e.g.*, chalcosite (Cu_2S),[23] digenite ($Cu_{1.8}S$),[24] tetrahedrite ($Cu_{12}Sb_4S_{13}$),[25,26] and colusite ($Cu_{26}T_2M_6S_{32}$ (T = Ti, V, Nb, Ta, Cr, Mo, W; M = Ge, Sn, Sb))[27–33] with ZT reaching ~0.5–1 at 673 K. However, less effort has been devoted to the fabrication of TE devices/modules[34–36] unlike the Mg-based compounds[37–39] and Half-Heusler compounds.[11,13,40] To maximize the conversion efficiency of a TE module, it is crucial to minimize the electrical and thermal contact resistance between the TE material and the electrodes that connect the devices in series. It is often necessary to insert interface materials between the TE material and the electrode, and identification of the more suitable materials is critically important.

[a]Interdisciplinary Graduate School of Engineering Sciences, Kyushu University, Kasuga, Fukuoka 816-8580, Japan. E-mail: suekuni.koichiro.063@m.kyushu-u.ac.jp

[b]Transdisciplinary Research and Education Center for Green Technologies, Kyushu University, Kasuga, Fukuoka 816-8580, Japan

[c]Department of Materials, Faculty of Engineering, Kyushu University, Motooka, Fukuoka 819-0395, Japan

[d]Université de Lorraine, CNRS, IJL, Nancy, F-54000, France

[e]Global Zero Emission Research Center, National Institute of Advanced Industrial Science and Technology (AIST), Tsukuba, Ibaraki 305-8569, Japan

[f]CRISMAT, CNRS, Normandie Université, ENSICAEN, UNICAEN, Caen 14000, France

We have recently discovered a colusite, $Cu_{26}Ti_2Sb_6S_{32}$, which showed semiconducting properties and low κ_{lat}.[32] The substitution of Ge^{4+} for Sb^{5+} increased the hole carrier concentration, n, leading to the enhancement of $S^2\rho^{-1}$. The combination of large $S^2\rho^{-1}$ and low κ_{lat} resulted in a ZT value of 0.9 at 673 K. From our subsequent investigations on $Cu_{26}Ti_2Sb_{6-x}Ge_xS_{32}$, we found that the previously studied samples[32] most probably present sulphur deficiency due to inadequate recovery of the sulphur residuals produced during the synthesis (reaction) process. In this study, we therefore investigated how the sulphur deficiency affects the crystal structure, electronic structure, and TE properties through experiments and *ab initio* calculations.

We then fabricated TE devices using the $Cu_{26}Ti_2Sb_{6-x}Ge_xS_{32}$ colusites. In our previous study,[34] we explored diffusion barrier materials from pure metals and reported that a single-leg device of $Cu_{26}Nb_2Ge_6S_{32}$ with Au layers (diffusion barrier layers) showed low contact resistance at the Au/colusite interface and a TE conversion efficiency of 3.3% at a temperature difference of $\Delta T \sim 270$ K. However, an issue arose from the macroscopic diffusion of Au into the colusite matrix. Specifically, the ΔV generated from the device was lower than the ΔV predicted based on the material's properties. Continued efforts are required to address this issue, while the exploration of diffusion barrier/interface materials holds comparable importance. In this study, we selected Ni as a diffusion barrier material. Ni is known to be reluctant to interdiffuse with Ag,[41] which is often used as a paste/electrode material. However, direct hot-press bonding between $Cu_{26}Ti_2Sb_{6-x}Ge_xS_{32}$ colusites and Ni was unsuccessful due to a reaction between the materials. Consequently, we explored interface materials to be placed between the colusite and Ni. As effective interface materials often share elements with TE materials (*e.g.*, MgCuSb for MgAgSb, $NiTe_2$ for $Bi_{0.5}Sb_{1.5}Te_3$, and CoAl for $CoSb_3$),[42] we selected Sb-based compounds, more specifically the Ni–Sb system (NiSb and $NiSb_2$) with metallic properties,[43] as potential candidates of interface materials for the colusite containing Sb.

2 Experimental procedures

2.1 Sample synthesis and device fabrication

We synthesized the samples with compositions of $Cu_{26}Ti_2Sb_4Ge_2S_{32-x}$ ($x = 0$, 0.5, 1.0, 1.5). The elements (Cu, 99.99%, wire; Ti, 99.99%, powder; Sb, 99.9999%, grain; S, 99.99%, powder) were sealed in an evacuated quartz tube. The tube was heated to 1173 K, maintained at this temperature for 24 h, and subsequently cooled to room temperature (RT). Yellow solids (sulphur) remaining in the quartz tube were thoroughly collected. The reaction product and sulphur were manually crashed and mixed using an agate mortar and then molded into a pellet by cold pressing. The pellet was sealed in an evacuated quartz tube and subjected to heat treatment at 823 K for 50 h. The annealed sample was manually crushed and then pulverized by using a planetary ball mill (Pulverisette 7 premium line, Fritsch) at a disk rotation speed of 450 rpm for 1 h. The powder was ball-milled in a jar with an inner volume of 20 mL together with seven balls of 10 mm diameter in an Ar atmosphere. The jar and balls were made of tungsten carbide (WC). The obtained powder was loaded into a WC die with an inner diameter of 10 mm, which was placed in a sintering furnace (PLASMAN CSP-I-03121, S. S. Alloy). Hot-press sintering was performed at 773 K for 1 h in a flowing N_2 atmosphere under a uniaxial pressure of 200 MPa. The sintered sample was cut and polished into bars and disks for the measurement of TE properties. The relative density d of samples was evaluated as $100 \times d_s/d_t$ in %, where d_s is the bulk density and d_t is the crystal density calculated as the ratio of the mass of a unit cell based on the starting composition ($Cu_{26}Ti_2Sb_4Ge_2S_{32-x}$) to the unit cell volume obtained from the X-ray diffraction analysis (Section 3.1).

Ni–Sb compounds (NiSb, $NiSb_2$, and Cu/Co-substituted NiSb: $Ni_{0.9}Cu_{0.1}Sb$ and $Ni_{0.9}Co_{0.1}Sb$) were synthesized by directly reacting the elements (Ni, 99.9%, powder; Co, 99.9%, powder; Cu, 99.9%, powder; Sb, 99.9999%, powder). The elements were mixed and then molded into a pellet, which was sealed in an evacuated quartz tube. The pellet was heated to 1323 K, maintained at this temperature for 24 h, cooled to 873 K, maintained at this temperature for 100 h, and then cooled to RT.

The powders of $Cu_{26}Ti_2Sb_4Ge_2S_{31.5}$ (ball-milled), Ni–Sb based compounds, and Ni were placed in a WC die to form 5 layers in the order Ni/Ni–Sb/$Cu_{26}Ti_2Sb_4Ge_2S_{31.5}$/Ni–Sb/Ni and hot-pressed under the aforementioned conditions to fabricate the TE devices. The obtained pellet was cut and polished into bars for the measurement of power generation properties.

2.2 Characterization

The crystal phases in the sintered samples of $Cu_{26}Ti_2Sb_4Ge_2S_{32-x}$ ($x = 0$, 0.5, 1.0, 1.5) and the samples of Ni–Sb-based compounds were identified by powder X-ray diffraction (PXRD). The PXRD data were collected in the range $10° \leq 2\theta \leq 100°$ using a diffractometer (Miniflex600, RIGAKU) with a CuKα radiation source. The lattice parameters were obtained by the Rietveld analysis using a program (Rietan-FP).[44] High-temperature PXRD measurements were performed using a heating stage (BTS500, Anton Paar) equipped in the diffractometer under a flowing N_2 atmosphere up to 573 K to investigate lattice parameter evolution. More detailed phase identification was performed for the colusite samples. The data were collected in the range $5° \leq 2\theta \leq 120°$ using a diffractometer (D8 Advance, Bruker) with a CuKα_1 (Ge(111) monochromator) radiation source. The data were analysed by Rietveld refinement using the FullProf and WinPlotr software packages.[45,46]

The surface morphologies and chemical compositions of the sintered samples were investigated by scanning electron microscopy (SEM) and energy dispersive X-ray spectroscopy (EDS). SEM and EDS were performed using a microscope (JCM-6000Plus NeoScope, JEOL).

2.3 Electrical and thermal property measurements and thermoelectric conversion efficiency evaluation

ρ and S were simultaneously measured by a four-probe DC method and a temperature differential method, respectively, at $T = 300$–673 K under a low-pressure He atmosphere using

a measurement system (ZEM-3, ADVANCE RIKO). The Hall-effect measurement was performed using a four-probe (Hall-bar geometry) DC method using a laboratory-built system with a permanent magnet generating a magnetic field of 0.63 T at RT. We calculated the carrier concentration n as $R_H^{-1}e^{-1}$, based on the single-carrier model, where R_H is the Hall coefficient and e is the elementary charge, respectively. Thermal diffusivity (α) was measured at $T = 300$–673 K in a flowing Ar atmosphere using a light flash apparatus (LFA-467 HT HyperFlash, Netzsch). These data were used to calculate $\kappa = \alpha C_{DP} d_s$, where C_{DP} is the Dulong–Petit value of specific heat. κ data for previously synthesized "$Cu_{26}Ti_2Sb_4Ge_2S_{32}$" shown in this paper were recalculated using C_{DP}.

The resistance scanning measurement was performed for the device composed of $Cu_{26}Ti_2Sb_4Ge_2S_{31.5}$, Ni–Sb-based compounds, and Ni by a four probe AC method using a laboratory-built system with a movable voltage probe. The TE conversion efficiency η of the device was evaluated in a vacuum using a measurement system (Mini-PEM, ADVANCE RIKO). η was calculated as $P/(P + Q_{out})$, where P is the output power and Q_{out} is the heat released into the low-temperature heat bath through the sample. In this measurement, the hot-side temperature of the device was set at $T_H = 321$–566 K, while keeping the cold-side temperature at $T_C = 295$–300 K.

2.4 Electronic structure calculations

Ab initio calculations were performed for $Cu_{26}Ti_2Sb_6S_{32}$ and two derivative compositions incorporating a S vacancy ($Cu_{26}Ti_2Sb_6S_{31}\square$, $\square$: vacancy) or an interstitial Cu ($Cu_{27}Ti_2Sb_6S_{32}$), as described below. The plane-wave-basis projector augmented wave (PAW) method[47] implemented in the Vienna *Ab initio* Simulation Package[48,49] was used. To model exchange–correlation effects, we employed the Perdew–Burke–Ernzerhof (PBE) functional[50] within the generalized gradient approximation (GGA). To treat the interactions among localized 3d electrons in Cu, the GGA + U scheme[51] was used, with a U value of 4.2 eV.[52] The valence configurations of the PAW potentials are as follows: [$3d^{10}$ $4s^1$] for Cu, [$3s^2$ $3p^6$ $3d^3$ $4s^1$] for Ti, [$5s^2$ $5p^3$] for Sb, and [$3s^2$ $3p^4$] for S. The remaining electrons were treated as frozen core electrons. The criterion for total energy convergence in the self-consistent electronic loop was set to 1.0×10^{-6} eV cell^{-1}. For structure optimization, atomic positions and lattice parameters were relaxed until atomic residual forces were $<5.0 \times 10^{-3}$ eV Å^{-1}. The first Brillouin zone was sampled using Monkhorst–Pack k-point grids of $4 \times 4 \times 4$,[53] and the plane-wave energy cutoff was set at 420 eV.

We performed the calculations for pristine $Cu_{26}Ti_2Sb_6S_{32}$, $Cu_{26}Ti_2Sb_6S_{31}\square$, and $Cu_{27}Ti_2Sb_6S_{32}$. The cubic structure (space group $P\bar{4}3n$, no. 218) of $Cu_{26}Ti_2Sb_6S_{32}$ includes non-equivalent crystallographic sites: three for Cu (6*d*, 8*e*, 12*f*), one for Ti (2*a*), one for Sb (6*c*), and two for S (8*e*, 24*i*).[32,54] One S atom at 8*e* or 24*i* was removed from the crystal structure to construct two $Cu_{26}Ti_2Sb_6S_{31}\square$ models, whereas one additional Cu atom was placed at unoccupied "interstitial" sites (6*b*, 24*i*) to construct two $Cu_{27}Ti_2Sb_6S_{32}$ models. The electronic band structures and density of states (DOS) were calculated for the five optimized structural models. For the band structure calculations, the reciprocal path for $Cu_{26}Ti_2Sb_6S_{32}$, as suggested by SeeK-path,[55] was applied to all models. This approach enables direct comparison of the electronic structures of the pristine and defect-containing models, although the defects break the original symmetry of $Cu_{26}Ti_2Sb_6S_{32}$. For the DOS calculations, a Γ-centred k-point mesh of $9 \times 9 \times 9$ was employed. Note that, in our calculations, two electrons per f.u. were intentionally removed to adjust the number of hole carriers in these non-Ge-substituted models to those for experimental Ge-substituted composition $Cu_{26}Ti_2Sb_4Ge_2S_{32-x}$. This procedure is useful to exclude the influence of interactions between Ge and other defects and to facilitate a concise discussion of sulphur deficiency.

The formation energies of a Cu interstitial and an S vacancy were calculated from the energy differences between the defect models and the pristine model, where two electrons were removed from both models, while including the chemical potentials of Cu or S to account for the exchange of these atoms with their reservoirs (*i.e.*, the competing phases). The chemical potentials of Cu and S were determined from the equilibrium conditions in the computed phase diagram.

3 Results & discussion

3.1 Crystal structure and chemical composition

PXRD patterns of $Cu_{26}Ti_2Sb_4Ge_2S_{32-x}$ ($x = 0$, 0.5, 1.0, 1.5) samples (after hot pressing) are shown in Fig. 1. For the $x = 0$ and $x = 0.5$ samples, all the diffraction peaks were indexed to the colusite structure (cubic, $P\bar{4}3n$), suggesting single phase samples, but the peaks were accompanied by a small shoulder at the lower angle side (Fig. S1). This result suggests inhomogeneous composition distribution. The peak asymmetry could be reproduced by assuming the existence of two colusite phases with and without Ge. For the $x = 0$ sample, the chemical compositions/fractions obtained by the Rietveld analysis were $Cu_{26}Ti_2Sb_{3.4(1)}Ge_{2.6(1)}S_{32}$/~94 wt% and $Cu_{26}Ti_2Sb_{6.0(1)}Ge_{0.0(1)}S_{32}$/~6 wt%. The former phase has a smaller lattice parameter, a, (10.7157(1) Å) than the latter phase (10.7536(3) Å), which probably results from the smaller ionic radius of Ge^{4+} compared to Sb^{5+}. Another possibility is that the composition distribution is linked to the formation of sulphur-deficient (Cu-rich) colusite (see Section 3.3). In any case, the amount of the secondary phase is likely to be small. A similar result was obtained for the $x = 0.5$ sample. Such a shoulder, if it exists, could not be detected in the PXRD patterns for the $x = 1.0$ and $x = 1.5$ samples. The Rietveld refinements indicated that the $x = 1.0$ sample was composed of a single colusite phase, whereas the $x = 1.5$ sample is composed of colusite and small amount of tetrahedrite ($Cu_{12}Sb_4S_{13}$, <2 wt%). The traces of secondary phases (Ge-poor or sulphur-deficient colusite for $x = 0$ and $x = 0.5$, and tetrahedrite for $x = 1.5$) in the samples should have minor effects on the TE properties.

The most prominent variation with x was an increase in a from 10.714 Å ($x = 0$, primary colusite phase) to 10.757 Å ($x = 1.5$). It should be noted that the sulphur deficiency was hard to be confirmed by the Rietveld analysis due to the strong interaction between the site occupation factors and the thermal

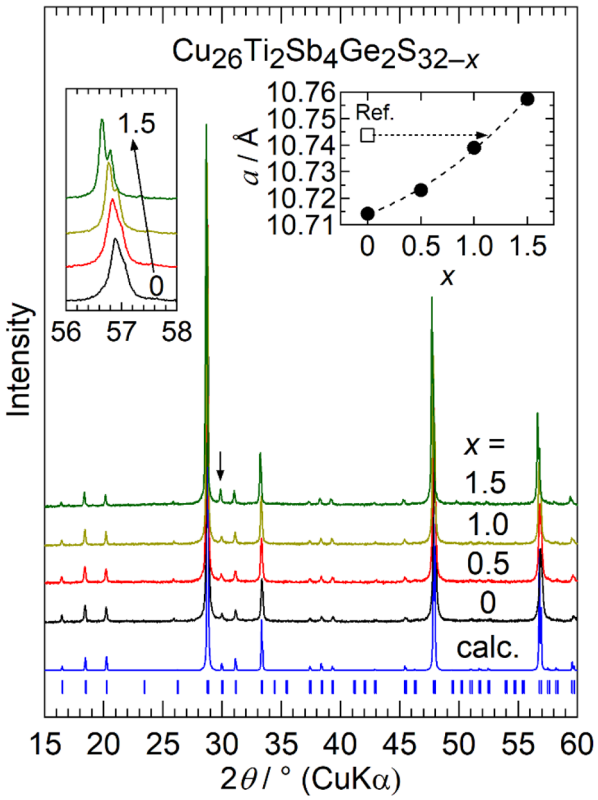

Fig. 1 X-ray diffraction patterns for the samples of $Cu_{26}Ti_2Sb_4Ge_2S_{32-x}$ ($x = 0$, 0.5, 1.0, 1.5). A simulated pattern for $Cu_{26}Ti_2Sb_6S_{32}$ and the peak position for CuKα radiation are shown at the bottom. An arrow indicates a peak from $Cu_{12}Sb_4S_{13}$. The left inset shows the expanded views of the 622 peaks. The right panel shows the lattice parameter, a, as a function of x. The closed circles are the data in this study and the open square indicates the data of "$Cu_{26}Ti_2Sb_4Ge_2S_{32}$" in our previous study (see text).

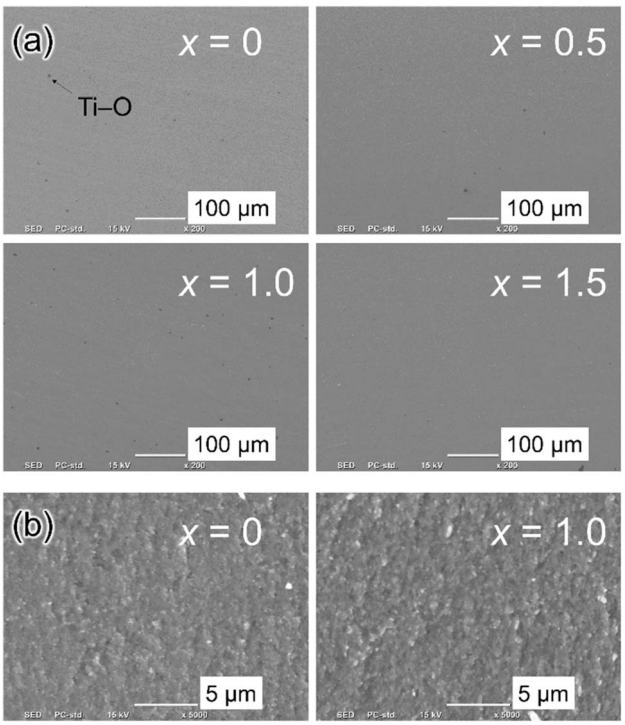

Fig. 2 Secondary electron images for (a) polished surfaces of the $Cu_{26}Ti_2Sb_4Ge_2S_{32-x}$ ($x = 0$, 0.5, 1.0, 1.5) samples and (b) fractured surfaces of the $x = 0$ and $x = 1$ samples.

parameters. Instead, EDS showed that the content of sulphur decreased with x, while those of cations (Cu, Ti, Sb, and Ge) were close to their nominal values (Table S1). It is noteworthy that the value of a for the previously synthesized "$Cu_{26}Ti_2Sb_4Ge_2S_{32}$" sample[32] was between those for the $x = 1.0$ and $x = 1.5$ samples of $Cu_{26}Ti_2Sb_4Ge_2S_{32-x}$ (inset of Fig. 1). This fact suggests sulphur deficiency in the previously synthesized sample. The defect species that are preferentially generated (sulphur vacancies or interstitial cations), their crystallographic sites, and the mechanism of lattice expansion were investigated by *ab initio* calculations (see Section 3.3).

3.2 Characteristics of bulk ceramics and thermoelectric properties

The TE properties were measured for the sintered samples, whose dense characteristics were proved by SEM (Fig. 2). The values of d were ~99% for $x = 0$ and $x = 0.5$, whereas ~101% and ~103% for $x = 1.0$ and $x = 1.5$, respectively. The samples were indeed dense, but the latter excessive densities raised questions about the validity of the assumed compositions (starting compositions). The causes of this result are discussed in Section 3.3. SEM images of the fractured surface for the $x = 0$ and $x = 1$ samples showed that the grain size was less than 1 μm (Fig. 2). The relatively small grain size is attributed to the ball-milling process before sintering.

Fig. 3 displays the TE properties for $Cu_{26}Ti_2Sb_4Ge_2S_{32-x}$ ($x = 0$, 0.5, 1.0, 1.5) and previously synthesized "$Cu_{26}Ti_2Sb_4Ge_2S_{32}$".[32] The $x = 0$ sample exhibited metallic behaviour in S and ρ (Fig. 3a and b). The values of S and ρ increased with increasing x, indicating a decrease in n. Indeed, the value of n obtained from Hall effect measurements at RT decreased from 3.5×10^{21} cm^{-3} ($x = 0$) to 2.4×10^{21} cm^{-3} ($x = 0.5$), 1.8×10^{21} cm^{-3} ($x = 1.0$) and 0.9×10^{21} cm^{-3} ($x = 1.5$). A similar trend in the electronic properties associated with sulphur deficiency was observed for colusite $Cu_{26}Cr_2Ge_6S_{32-\delta}$.[31] The values of $S^2\rho^{-1}$ for $Cu_{26}Ti_2Sb_4Ge_2S_{32-x}$ were equal to 1.4 mWK^{-2} m^{-1} at 673 K for the $x = 0$–1.0 samples, whereas it decreased to 0.97 mWK^{-2} m^{-1} for the $x = 1.5$ sample (Fig. 3c). The decrease in n with x led to the reduction in the electronic thermal conductivity, κ_{ele} (Table S2). As a result, the value of κ at 673 K decreased from 1.3 WK^{-1} m^{-1} ($x = 0$) to 0.62 WK^{-1} m^{-1} ($x = 1.5$) (Fig. 3d). The lattice thermal conductivity κ_{lat} was estimated by subtracting κ_{ele} from κ. Here the values of κ_{ele} were estimated from the Wiedemann–Franz law, $\kappa_{ele} = LT\rho^{-1}$, where the Lorentz number L was calculated using an equation, $L = 1.5 + \exp(-|S|/116)$, based on a single parabolic band model with acoustic phonon scattering.[56] In the lower temperature region, κ_{lat} values for the $x \geq 0.5$ samples were equivalent and slightly lower than that for the $x = 0$ sample (Fig. 3e). Because the morphology of the sample (grain size) was similar between $x =$

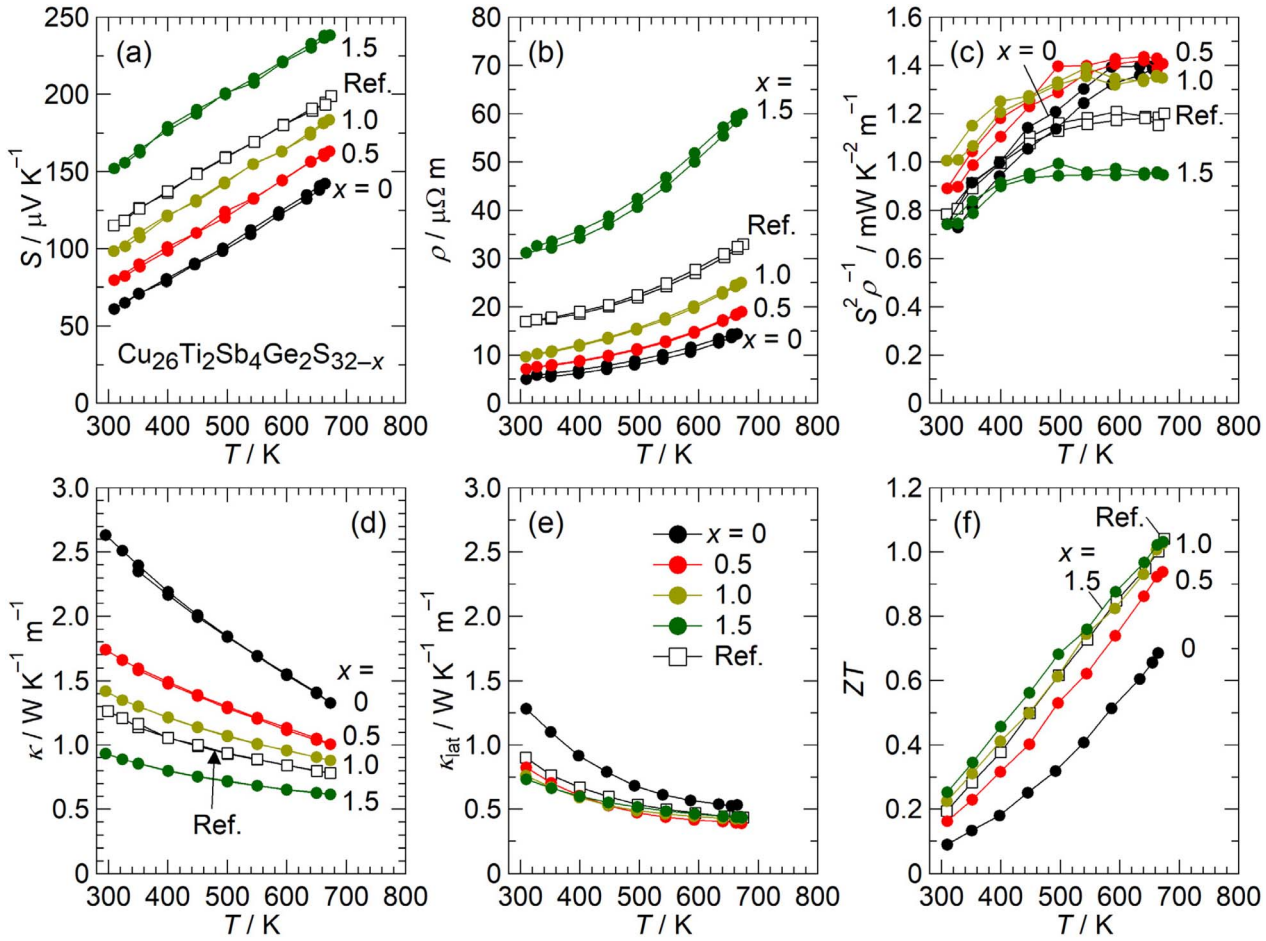

Fig. 3 (a) Seebeck coefficient, S, (b) electrical resistivity, ρ, (c) power factor, $S^2\rho^{-1}$, (d) thermal conductivity, κ, (e) lattice thermal conductivity, κ_{lat}, and (f) dimensionless figure of merit, ZT, for the samples of $Cu_{26}Ti_2Sb_4Ge_2S_{32-x}$ (x = 0, 0.5, 1.0, 1.5). The closed circles are the data in this study and the open squares indicate the data of "$Cu_{26}Ti_2Sb_4Ge_2S_{32}$" in our previous study (see text).

0 and $x = 1.0$, as mentioned above (Fig. 2), the κ_{lat} reduction can be attributed to the structural modification due to sulphur deficiency (see Section 3.3). The combination of high $S^2\rho^{-1}$ and low κ led to relatively high ZT, which increased from 0.7 ($x = 0$) to 0.9 ($x = 0.5$) and 1.0 ($x = 1.0$, 1.5) at 673 K (Fig. 3f). The values of ρ, S, κ as well as ZT for the previously synthesized "$Cu_{26}Ti_2Sb_4Ge_2S_{32}$"[32] were between those for $x = 1.0$ and $x = 1.5$ (Fig. 3), consistent with the XRD results, as discussed above.

3.3 Possible defects

We performed *ab initio* calculations for the pristine model ($Cu_{26}Ti_2Sb_6S_{32}$), two sulphur vacancy models ($Cu_{26}Ti_2Sb_6S_{31}\square$), and two Cu interstitial models ($Cu_{27}Ti_2Sb_6S_{32}$) (see Section 2.4). In these calculations, two electrons were intentionally removed from the models to simulate the hole concentration of the experimentally Ge-substituted samples. As a result, the pristine model exhibited a p-type degenerate semiconducting electronic structure (Fig. 4 and S2), consistent with the metallic properties observed in $Cu_{26}Ti_2Sb_4Ge_2S_{32}$ (Fig. 3).

First, we compared the stability of two sulphur vacancies at two different sites. The formation energy of a sulphur vacancy at the 8*e* site was found to be higher (+1.8 eV) than that at the 24*i* site,

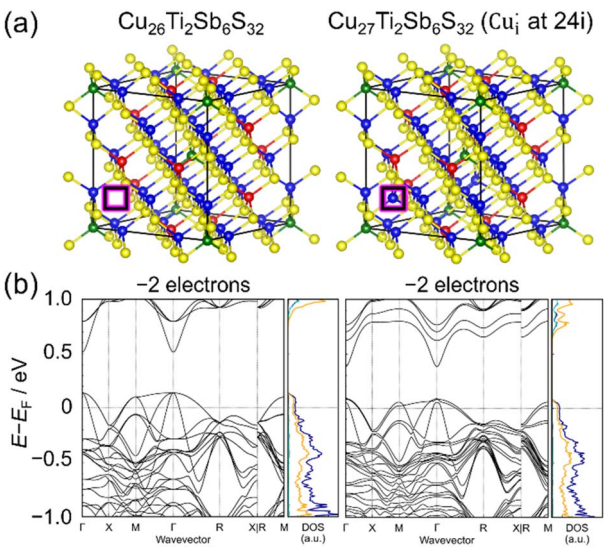

Fig. 4 (a) Relaxed structures of $Cu_{26}Ti_2Sb_6S_{32}$ and $Cu_{27}Ti_2Sb_6S_{32}$. For the latter, a copper atom was placed at the 24*i* (interstitial) site. (b) Electronic band dispersion relations and element-projected density of states for $Cu_{26}Ti_2Sb_6S_{32}$ and $Cu_{27}Ti_2Sb_6S_{32}$.

indicating that the 8*e*-site vacancy is energetically less favourable. Because the 8*e* site locates in a rigid $[TiS_4]Cu_6$ tetrahedral–octahedral complex,[30,54] vacancy formation at this site is not preferred. The electronic structure of $Cu_{26}Ti_2Sb_6S_{31}\square$ with the 24*i*-site sulphur vacancy exhibits degenerate semiconducting characteristics similar to those of $Cu_{26}Ti_2Sb_6S_{32}$ (Fig. S2). This result was contrary to our initial anticipation that a neutral sulphur vacancy would lead to electron doping. The relaxed structure (Fig. S3) and the orbital projected DOS for Sb (Fig. S4) suggest that the neutral sulphur vacancy on 24*i* site induces the formation of a $5s^2$ lone pair in Sb, thereby reducing the valence state of Sb from +5 to +3. Considering that Sb atoms are in tetrahedral coordination of S(24*i*) in colusite, it is reasonable to consider that the lone pair of the Sb^{3+} cation compensate the sulphur vacancy to form an $SbS(24i)_3LP$ polyhedron. Furthermore, only a slight increase in the calculated lattice parameter *a* (~0.002 Å) was observed after removing the sulphur atom from the 24*i* site, which disagrees with the increase of lattice parameter, determined from the XRD analyses (Fig. 1). In addition, the localization of two electrons from the sulphur vacancy prevents any decrease in hole concentration, as evidenced by the unchanged Fermi level relative to the valence band maximum (Fig. S2). This result is also inconsistent with the experimental values of *n* decreasing with *x* (Fig. 3), suggesting that sulphur vacancy formation is unlikely under our synthesis conditions.

According to our previous studies,[57] sulphur deficiency (volatilization) is compensated by the incorporation of cations into the unoccupied interstitial 24*i* site of the sphalerite-like framework of colusite. Indeed, an interstitial Cu atom at the 24*i* site (Fig. 4a) is energetically more favourable than one at the 6*b* site, with a calculated formation energy lower by 0.17 eV. The 24*i*-site interstitial caused an increase in the calculated *a* of 0.030 Å, which is significantly larger than that of the sulphur vacancy model and agrees with the experimental observations (Fig. 1). A Cu-excess composition/structure, if present, explains the geometrical densities exceeding 100% of the theoretical ones (*i.e.* without interstitial cations, Section 3.2). In addition, the number of hole carriers decreased as the Fermi level shifts toward the band edge to maintain charge balance (Fig. 4b), which is consistent with the measured TE properties (Fig. 3). Therefore, structural modifications due to Cu interstitials probably occurred in the $Cu_{26}Ti_2Sb_4Ge_2S_{32-x}$ ($x > 0$) samples. Indeed, the formation energy of a Cu interstitial is lower than that of an S vacancy under all equilibrium conditions in the computed phase diagram. For example, under an S-poor condition in equilibrium with $Cu_{12}Sb_4S_{13}$, Cu_7S_4, and Cu_2S, the formation energies are 0.23 eV and 0.53 eV, respectively. This indicates that Cu interstitials are more readily formed than S vacancies in the colusite. It is noteworthy that the value of κ_{lat} near the room temperature was reduced at $x > 0$ (Fig. 3e). This result indicates that the interstitial Cu acts as a phonon scattering center, as reported previously.[57,58]

3.4 Device characterization

TE devices composed of colusite ($Cu_{26}Ti_2Sb_4Ge_2S_{31.5}$, *i.e.*, $x = 0.5$), Ni–Sb, and Ni layers were fabricated as described in Section 2.1. The device containing $NiSb_2$ was fractured while being removed from the die after sintering (Fig. 5a), whereas the device with NiSb was successfully fabricated (Fig. 5b). The coefficient of volumetric thermal expansion of NiSb (4.56×10^{-5} K^{-1}), calculated from the temperature dependence of lattice parameters between 300 K and 573 K (Fig. 5c and S5), was comparable to that of the colusite (4.82×10^{-5} K^{-1}). In contrast, the value of thermal expansion for $NiSb_2$ (3.43×10^{-5} K^{-1}) was significantly smaller. The well-matched thermal expansion coefficients are likely responsible for the observed crack-free NiSb/colusite interface (Fig. 5b). However, resistance scanning data for the device with NiSb exhibited a large step (contact resistivity, R_c) of ~13 mΩ mm^2 at the NiSb/colusite interface as shown in Fig. 5d. The sum of R_c at both sides of the device equals to ~33% of cumulative electrical resistivity of the device. Conversely, R_c between Ni and NiSb was negligibly small. It is noteworthy that the linear trend in the resistance scanning data within the colusite layer indicates its chemical composition homogeneity.

We then investigated how chemical substitution in NiSb influences R_c. The devices containing Cu- and Co-substituted NiSb showed no crack near the interfaces between the NiSb-based compounds and the colusite (Fig. S6). The devices with $Ni_{0.9}Cu_{0.1}Sb$ and $Ni_{0.9}Co_{0.1}Sb$ exhibited, respectively, higher R_c (~30, ~50 mΩmm^2) and lower R_c (~9 mΩmm^2) at the NiSb-based compounds/colusite interfaces compared to the device with NiSb (Fig. 5d). The interfaces were analysed by SEM (Fig. S7). For the devices containing NiSb and $Ni_{0.9}Cu_{0.1}Sb$, thin NiSbS, Sb_2S_3, and multiphase layers were formed. Conversely, for the device with $Ni_{0.9}Co_{0.1}Sb$, only small amounts of (Ni,Co)SbS and Sb_2S_3 were detected. The NiSbS layer likely forms through the sulphurization of NiSb. Given that NiSbS itself possesses metallic characteristics,[59] the formation of the Sb_2S_3 layer is primarily responsible for the increase in R_c (Fig. 5d). In devices containing $Ni_{0.9}Co_{0.1}Sb$, the presence of a small amount of Sb_2S_3 should be responsible for a non-negligible R_c.

The R_c value for the device with $Ni_{0.9}Co_{0.1}Sb$ was ~9 mΩ mm^2 (Fig. 5d). The R_c remained nearly constant after annealing at 573 K for 50 h, but increased significantly as the annealing temperature was elevated to 623 K and 673 K (Fig. S8). After annealing, a thin (Ni,Co)SbS layer formed and its thickness increased with elevating the annealing temperature (Fig. S9). Its metallic characteristics would have limited impact on R_c. For the sample annealed at 673 K, Sb_2S_3 was clearly visible in a SEM image (Fig. S9). Therefore, the formation of Sb_2S_3 is primarily responsible for the observed increase in R_c, which is consistent with the claim made above.

For the unannealed device containing $Ni_{0.9}Co_{0.1}Sb$, the ρ value, estimated from the slope of the resistance scanning data, was 9.7 Ω m at RT. This value was slightly higher than that for $x = 0.5$ of $Cu_{26}Ti_2Sb_4Ge_2S_{32-x}$ (colusite used for the devise, $Cu_{26}Ti_2Sb_4Ge_2S_{31.5}$) but was comparable to that for $x = 1.0$ (Fig. 3b). The increase in ρ for the colusite phase was probably attributed to a decrease in sulphur content due to the reaction between the colusite and $Ni_{0.9}Co_{0.1}Sb$ during the sintering. We therefore compared the experimental power generation properties for the device to simulate results based on the TE properties of $x = 1.0$ (Fig. S10 and Tables S3, S4).

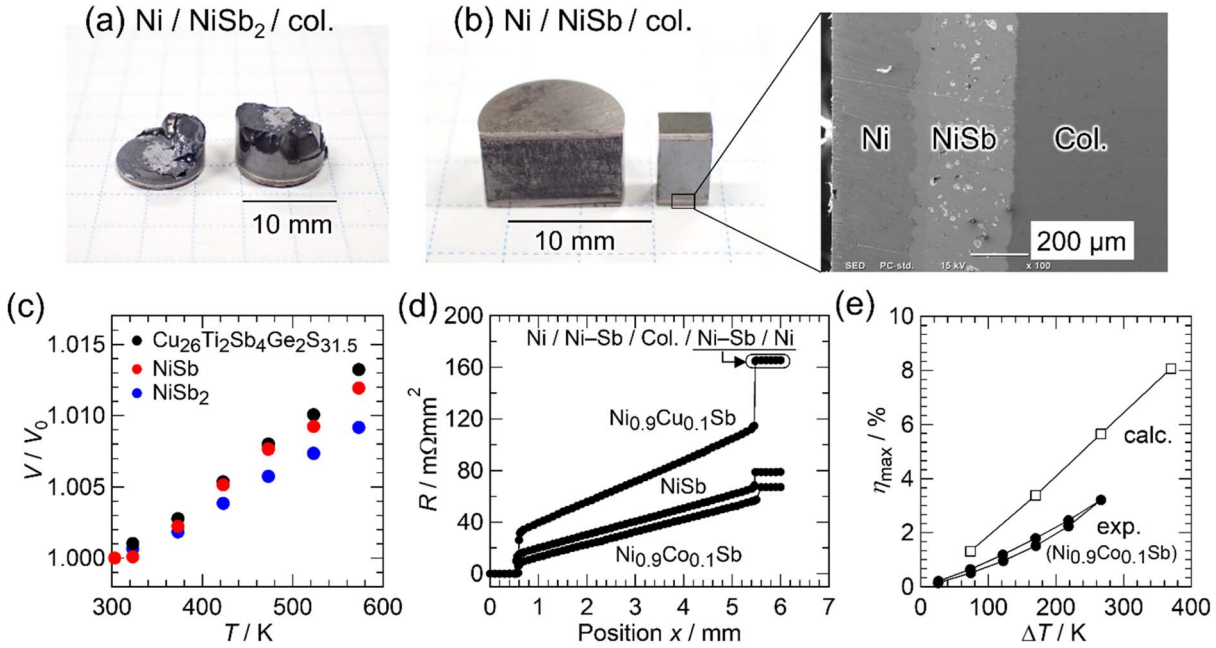

Fig. 5 Sintered samples composed of (a) Ni, $NiSb_2$, and $Cu_{26}Ti_2Sb_4Ge_2S_{31.5}$ (col.) layers and (b) Ni, NiSb, and col. layers. In (b), a secondary electron image of one end of the device is shown. (c) Temperature dependence of unit cell volumes normalized at 300 K for $Cu_{26}Ti_2Sb_4Ge_2S_{31.5}$, $NiSb_2$, and NiSb. (d) Cumulative electrical resistivity, R, for the devices composed of Ni, NiSb-based compounds, and $Cu_{26}Ti_2Sb_4Ge_2S_{31.5}$ (col.). (e) Temperature dependences of maximum conversion efficiency, η_{max}, for the device with $Ni_{0.9}Co_{0.1}Sb$. The calculated η_{max} based on the TE properties of $Cu_{26}Ti_2Sb_4Ge_2S_{32-x}$ ($x = 1.0$) is also shown in (e).

The power generation properties of the device with $Ni_{0.9}Co_{0.1}Sb$ were investigated with T_H reaching up to 573 K, while T_C was maintained at ~300 K (Fig. 5e and S11). The maximum output power, P_{max}, obtained from the voltage–current plot increased with increasing temperature difference ΔT and reached 23 mW at $\Delta T = 266$ K (Fig. S11a and b). It should be noted that the open circuit voltage V_{oc} and internal resistance R_{in} were reversible between the heating and cooling processes (Fig. S11c and d), indicating the device's stability under the current measurement conditions. $\eta_{max} = P/(P + Q_{out})$ increased with increasing ΔT and reached 3.2% at $\Delta T = 266$ K (Fig. 5e and S11e, f). This value is equivalent to η_{max} measured for a $Cu_{26}Nb_2Ge_6S_{32}$-based device (3.3%),[34] while is lower than that for Cu_2ZnSnS_4-based single crystals (4%).[60] η_{max} for an ideal device with the TE properties of $x = 1.0$, calculated using COMSOL Multiphysics® and a web simulator,[61] was 5.7% when T_L and T_H were set at 300 K and 573 K, respectively (Fig. 5e and Table S4). Because the V_{oc} values were comparable between the experiment and calculation, the reduced η_{max} for the fabricated device can be mainly attributed to the non-negligible contact resistance between the colusite and $Ni_{0.9}Co_{0.1}Sb$ (resulting in an increase in device resistance) and the consequent reduction in P (Fig. S11). The calculated η_{max} for $x = 1.0$ reached 8.1% at $\Delta T = 373$ K ($T_L = 300$ K, $T_H = 673$ K) (Fig. 5e), highlighting its high potential for TE applications. While this value is comparable to or still lower than other promising materials, *e.g.*, Mg-based compounds and Half-Heusler compounds,[11,13,37,38,40] $Cu_{26}Ti_2Sb_4Ge_2S_{32-x}$ could be a strong candidate for practical application if the interfacial material is optimized, given that its primary constituent elements (Cu and S) are low-toxicity, abundant elements.

4 Conclusions

In summary, we synthesized a series of polycrystalline colusites $Cu_{26}Ti_2Sb_4Ge_2S_{32-x}$ and addressed the role of sulphur deficiency in the crystal structure, electronic structure, and TE properties. From experimental data and *ab initio* calculations, we demonstrated that sulphur deficiency in the nominal composition induced the formation of "interstitial" Cu within the sphalerite-like framework, which resulted in lattice expansion and a decrease in the hole carrier concentration. Fine tuning of the carrier concentration led to a significant increase in ZT. We also explored interface materials derived from Ni–Sb-based compounds and fabricated a TE device composed of Ni, $Ni_{0.9}Co_{0.1}Sb$, and $Cu_{26}Ti_2Sb_4Ge_2S_{32-x}$, whose maximum conversion efficiency reached 3.2% at a temperature difference of 266 K. Further explorations of interface materials/diffusion barrier materials will open pathways for practical applications of Cu–S-based TE materials.

Author contributions

Koichiro Suekuni: conceptualization, data curation, funding acquisition, investigation, project administration, resources, supervision, visualization, writing – original draft, writing – review and editing. Mei Yamamoto: investigation, visualization, writing – review and editing. Susumu Fujii: investigation,

methodology, resources, funding acquisition, visualization, writing – review and editing. Pierric Lemoine: investigation, visualization, validation, writing – review and editing. Philipp Sauerschnig: data curation, investigation, writing – review and editing. Michihiro Ohta: data curation, funding acquisition, investigation, resources, writing – review and editing. Emmanuel Guilmeau: validation, writing – review and editing. Michitaka Ohtaki: resources, writing – review and editing.

Conflicts of interest

There are no conflicts to declare.

Data availability

The data supporting this article have been included as part of the supplementary information (SI). Supplementary information: powder X-ray diffraction patterns, chemical compositions, hole carrier concentration and total thermal conductivity at room temperature, electronic band dispersion relations and density of states, relaxed structures used for the calculations, temperature dependence of lattice parameters, secondary electron images of devices, resistivity scanning data, details of the finite-element method simulation, measured and calculated power generation properties. See DOI: https://doi.org/10.1039/d5ta08599c.

Acknowledgements

This work was financially supported by JSPS KAKENHI (grant no. JP24H00415 (K.S.), JP25K01503 (K.S.), and JP22H04914 (S.F.)), the Thermal and Electric Energy Technology Foundation (K.S.), the Research and Development Program for Promoting Innovative Clean Energy Technologies through International Collaboration funded by NEDO (grant no. JPNP20005 (M.Ohta and K.S.)), JST FOREST (grant no. JPMJFR235X (S.F.)), and JST CREST (grant no. JPMJCR25S3 (K.S.)).

References

1 R. Freer and A. V. Powell, *J. Mater. Chem. C*, 2020, **8**, 441–463.
2 H. Tamaki, H. K. Sato and T. Kanno, *Adv. Mater.*, 2016, **28**, 10182–10187.
3 K. Imasato, S. D. Kang and G. J. Snyder, *Energy Environ. Sci.*, 2019, **12**, 965–971.
4 A. Li, C. Fu, X. Zhao and T. Zhu, *Research*, 2020, **2020**, 1–22.
5 M. J. Kirkham, A. M. Dos Santos, C. J. Rawn, E. Lara-Curzio, J. W. Sharp and A. J. Thompson, *Phys. Rev. B: Condens. Matter Mater. Phys.*, 2012, **85**, 1–7.
6 H. Zhao, J. Sui, Z. Tang, Y. Lan, Q. Jie, D. Kraemer, K. McEnaney, A. Guloy, G. Chen and Z. Ren, *Nano Energy*, 2014, **7**, 97–103.
7 Z. Liu, J. Mao, J. Sui and Z. Ren, *Energy Environ. Sci.*, 2018, **11**, 23–44.
8 J. Tani and H. Kido, *Phys. B*, 2005, **364**, 218–224.
9 V. K. Zaitsev, M. I. Fedorov, E. A. Gurieva, I. S. Eremin, P. P. Konstantinov, A. Y. Samunin and M. V. Vedernikov, *Phys. Rev. B*, 2006, **74**, 045207.
10 J. de Boor, T. Dasgupta, U. Saparamadu, E. Müller and Z. F. Ren, *Mater. Today Energy*, 2017, **4**, 105–121.
11 T. Zhu, C. Fu, H. Xie, Y. Liu and X. Zhao, *Adv. Energy Mater.*, 2015, **5**, 1500588.
12 L. Huang, Q. Zhang, B. Yuan, X. Lai, X. Yan and Z. Ren, *Mater. Res. Bull.*, 2016, **76**, 107–112.
13 W. Li, S. Ghosh, N. Liu and B. Poudel, *Joule*, 2024, **8**, 1274–1311.
14 K. Suekuni and T. Takabatake, *APL Mater.*, 2016, **4**, 104503.
15 A. V. Powell, *J. Appl. Phys.*, 2019, **126**, 100901.
16 P. Lemoine, G. Guélou, B. Raveau and E. Guilmeau, *Angew. Chem., Int. Ed.*, 2022, **61**, e202108686.
17 Z. Ge, *Mater. Lab.*, 2022, **1**, 1–21.
18 M. Sahu and C. Park, *Mater. Today Sustain.*, 2023, **23**, 100441.
19 E. Guilmeau, A. Maignan, C. Wan and K. Koumoto, *Phys. Chem. Chem. Phys.*, 2015, **17**, 24541–24555.
20 P. Jood and M. Ohta, *Materials*, 2015, **8**, 1124–1149.
21 K. Hashikuni, K. Suekuni, H. Usui, M. Ohta, K. Kuroki and T. Takabatake, *Appl. Phys. Lett.*, 2016, **109**, 1–6.
22 K. Hashikuni, K. Suekuni, H. Usui, R. Chetty, M. Ohta, K. Kuroki, T. Takabatake, K. Watanabe and M. Ohtaki, *Inorg. Chem.*, 2019, **58**, 1425–1432.
23 Y. He, T. Day, T. Zhang, H. Liu, X. Shi, L. Chen and G. J. Snyder, *Adv. Mater.*, 2014, **26**, 3974–3978.
24 Y.-X. Zhang, J. Feng and Z.-H. Ge, *Chem. Eng. J.*, 2022, **428**, 131153.
25 X. Lu, D. T. Morelli, Y. Xia, F. Zhou, V. Ozolins, H. Chi, X. Zhou and C. Uher, *Adv. Energy Mater.*, 2013, **3**, 342–348.
26 K. Suekuni, K. Tsuruta, M. Kunii, H. Nishiate, E. Nishibori, S. Maki, M. Ohta, A. Yamamoto and M. Koyano, *J. Appl. Phys.*, 2013, **113**, 043712.
27 K. Suekuni, F. S. Kim, H. Nishiate, M. Ohta, H. I. Tanaka and T. Takabatake, *Appl. Phys. Lett.*, 2014, **105**, 132107.
28 Y. Kikuchi, Y. Bouyrie, M. Ohta, K. Suekuni, M. Aihara and T. Takabatake, *J. Mater. Chem. A*, 2016, **4**, 15207–15214.
29 Y. Bouyrie, M. Ohta, K. Suekuni, Y. Kikuchi, P. Jood, A. Yamamoto and T. Takabatake, *J. Mater. Chem. C*, 2017, **5**, 4174–4184.
30 V. Pavan Kumar, A. R. Supka, P. Lemoine, O. I. Lebedev, B. Raveau, K. Suekuni, V. Nassif, R. Al Rahal Al Orabi, M. Fornari and E. Guilmeau, *Adv. Energy Mater.*, 2019, **9**, 1803249.
31 G. Guélou, V. Pavan Kumar, A. Bourhim, P. Lemoine, B. Raveau, A. Supka, O. I. Lebedev, R. Al Rahal Al Orabi, M. Fornari, K. Suekuni and E. Guilmeau, *ACS Appl. Energy Mater.*, 2020, **3**, 4180–4185.
32 T. Hagiwara, K. Suekuni, P. Lemoine, A. R. Supka, R. Chetty, E. Guilmeau, B. Raveau, M. Fornari, M. Ohta, R. Al Rahal Al Orabi, H. Saito, K. Hashikuni and M. Ohtaki, *Chem. Mater.*, 2021, **33**, 3449–3456.
33 G. Guélou, P. Lemoine, B. Raveau and E. Guilmeau, *J. Mater. Chem. C*, 2021, **9**, 773–795.

34 R. Chetty, Y. Kikuchi, Y. Bouyrie, P. Jood, A. Yamamoto, K. Suekuni and M. Ohta, *J. Mater. Chem. C*, 2019, **7**, 5184–5192.
35 R. Chetty, P. Jood, M. Murata, K. Suekuni and M. Ohta, *Appl. Phys. Lett.*, 2022, **120**, 013501.
36 R. Coelho, Y. De Abreu, F. Carvalho, E. B. Lopes and A. P. Gonçalves, in *Materiais 2022*, MDPI, Basel Switzerland, 2022, p. 87.
37 Z. Liu, N. Sato, W. Gao, K. Yubuta, N. Kawamoto, M. Mitome, K. Kurashima, Y. Owada, K. Nagase, C.-H. Lee, J. Yi, K. Tsuchiya and T. Mori, *Joule*, 2021, **5**, 1196–1208.
38 P. Ying, R. He, J. Mao, Q. Zhang, H. Reith, J. Sui, Z. Ren, K. Nielsch and G. Schierning, *Nat. Commun.*, 2021, **12**, 1–6.
39 T. Nakamura, K. Hatakeyama, M. Minowa, Y. Mito, K. Arai, T. Iida and K. Nishio, *J. Electron. Mater.*, 2015, **44**, 3592–3597.
40 H. Zhu, W. Li, A. Nozariasbmarz, N. Liu, Y. Zhang, S. Priya and B. Poudel, *Nat. Commun.*, 2023, **14**, 1–8.
41 X. J. Liu, F. Gao, C. P. Wang and K. Ishida, *J. Electron. Mater.*, 2008, **37**, 210–217.
42 L. Xie, L. Yin, Y. Yu, G. Peng, S. Song, P. Ying, S. Cai, Y. Sun, W. Shi, H. Wu, N. Qu, F. Guo, W. Cai, H. Wu, Q. Zhang, K. Nielsch, Z. Ren, Z. Liu and J. Sui, *Science*, 2023, **382**, 921–928.
43 X.-N. Luo, C. Dong, S.-K. Liu, Z.-P. Zhang, A.-L. Li, L.-H. Yang and X.-C. Li, *Chin. Phys. B*, 2015, **24**, 067201.
44 F. Izumi and K. Momma, *Solid State Phenom.*, 2007, **130**, 15–20.
45 J. Rodríguez-Carvajal, *Phys. B*, 1993, **192**, 55–69.
46 T. Roisnel and J. Rodríquez-Carvajal, *Mater. Sci. Forum*, 2001, **378–381**, 118–123.
47 P. E. Blöchl, *Phys. Rev. B*, 1994, **50**, 17953–17979.
48 G. Kresse and J. Hafner, *Phys. Rev. B*, 1994, **49**, 14251–14269.
49 G. Kresse and J. Furthmüller, *Phys. Rev. B*, 1996, **54**, 11169–11186.
50 J. P. Perdew, K. Burke and M. Ernzerhof, *Phys. Rev. Lett.*, 1996, **77**, 3865–3868.
51 S. L. Dudarev, G. A. Botton, S. Y. Savrasov, C. J. Humphreys and A. P. Sutton, *Phys. Rev. B*, 1998, **57**, 1505–1509.
52 V. Pavan Kumar, S. Passuti, B. Zhang, S. Fujii, K. Yoshizawa, P. Boullay, S. Le Tonquesse, C. Prestipino, B. Raveau, P. Lemoine, A. Paecklar, N. Barrier, X. Zhou, M. Yoshiya, K. Suekuni and E. Guilmeau, *Angew. Chem., Int. Ed.*, 2022, **61**, e202210600.
53 J. D. Pack and H. J. Monkhorst, *Phys. Rev. B*, 1977, **16**, 1748–1749.
54 T. Hagiwara, K. Suekuni, P. Lemoine, C. Prestipino, E. Elkaim, A. R. Supka, R. Al Rahal Al Orabi, M. Fornari, E. Guilmeau, B. Raveau, H. Saito, P. Sauerschnig, M. Ohta, Y. Kanemori and M. Ohtaki, *Chem. Mater.*, 2023, **35**, 7554–7563.
55 Y. Hinuma, G. Pizzi, Y. Kumagai, F. Oba and I. Tanaka, *Comput. Mater. Sci.*, 2017, **128**, 140–184.
56 H.-S. Kim, Z. M. Gibbs, Y. Tang, H. Wang and G. J. Snyder, *APL Mater.*, 2015, **3**, 041506.
57 K. Suekuni, Y. Shimizu, E. Nishibori, H. Kasai, H. Saito, D. Yoshimoto, K. Hashikuni, Y. Bouyrie, R. Chetty, M. Ohta, E. Guilmeau, T. Takabatake, K. Watanabe and M. Ohtaki, *J. Mater. Chem. A*, 2019, **7**, 228–235.
58 Y. Shimizu, K. Suekuni, H. Saito, P. Lemoine, E. Guilmeau, B. Raveau, R. Chetty, M. Ohta, T. Takabatake and M. Ohtaki, *Inorg. Chem.*, 2021, **60**, 11364–11373.
59 M. Miyata, T. Ozaki, S. Nishino and M. Koyano, *Jpn. J. Appl. Phys.*, 2017, **56**, 021801.
60 A. Nagaoka, K. Nagatomo, K. Nakashima, Y. Hirai, Y. Ota, K. Yoshino and K. Nishioka, *Mater. Trans.*, 2023, **64**, 2535–2541.
61 Thermoelectric Power Generation Web Simulator Lite ver.0.53a, https://tes.keri.re.kr/.

